

## 2-D Statistical Damage Detection of Concrete Structures Combining Smart Piezoelectric Materials and Scanning Laser Doppler Vibrometry

Costas P. Providakis<sup>1,\*</sup>, Stavros E. Tsistrakis<sup>1</sup> and Evangelos V. Liarakos<sup>1</sup>

**Abstract:** In the present study a new structural health monitoring (SHM) technique is proposed as well as a new damage index based on 2-D error statistics. The proposed technique combines the electromechanical impedance technique (EMI) which is based on the use of piezoelectric Lead Zirconate Titanate (PZT) patches and Scanning Laser Doppler Vibrometry (SLDV) for damage detection purposes of concrete structures and early age monitoring. Typically the EMI technique utilizes the direct and inverse piezoelectric effect of a PZT patch attached to a host structure via an impedance analyzer that is used for both the actuation and sensing the response of the PZT-Host structure system. In the proposed technique the attached PZTs are actuated via a function generator and the PZT-Host structure response is obtained by a Scanning Laser Doppler Vibrometer. Spectrums of oscillation velocity of the surface of the attached PZTs vertical to the laser beam versus frequency are obtained and are evaluated for SHM purposes. This damage detection approach also includes the use of a damage index denoted as ECAR (Ellipse to Circle Area Ratio) based on 2-D error statistics and is compared to the Root Mean Square Deviation (RMSD) damage index commonly used in SHM applications. Experimental results include ascending uniaxial compressive load of concrete cubic specimens, ascending three point bending of reinforced concrete beam specimens and early age monitoring of concrete. Results illustrate the efficiency of the proposed technique in damage detection as well as early age monitoring as, in the first case, both severity and location of damage can be determined by examining the values of damage indices for each damaged state and in the early age monitoring case damage indices follow the strength gain curve.

**Keywords:** Concrete, damage detection, Scanning Laser Doppler Vibrometry, PZT, error statistics.

### 1 Introduction

Concrete is the most commonly used material in civil engineering infrastructure. Its low cost, durability, diversity in shape and meeting performance requirements are only a number of its advantages that have made it the dominant material used in construction. Although all the materials that concrete consists of are produced meeting strict standards,

---

<sup>1</sup> Technical University of Crete, School of Architecture, Kounoupidiana, Chania, GR 73100, Greece.

\* Corresponding Author: Costas P. Providakis. Email: cprov@mred.tuc.gr.

it is the concrete itself that has to meet certain properties, as it is usually made in situ in an uncontrolled environment. Additionally, with an expected lifetime of approximately 100 years, concrete structures have a long service life compared with other electrical or mechanical commercial products. So, the ambiguity as far as its initial properties is concerned, combined with its natural deterioration over time due to a number of reasons ranging from corrosion from environmental reasons to natural disasters such as earthquakes, make damage detection and evaluation of the structural integrity of concrete structures a matter of utmost importance.

The area of non-destructive evaluation (NDE) and structural health monitoring (SHM) is a very active scientific research field. Since the mid 90's a number of techniques can be found in the literature. Global dynamic techniques as well as various localized techniques such as ultrasonic wave propagation, impact echo, x ray radiography etc. have been used for NDE and SHM purposes. The main drawbacks of global dynamic techniques that rely on the first few natural modes of the structure is that they are insensitive to localized damage and are affected by the ambient noise due to low frequency excitation. The sensitivity of localized techniques is significantly higher than the global techniques, however they are difficult to employ especially on large scale structures, although their ability to detect damage has been well demonstrated.

Since the early 90's the development of the SHM and NDE techniques has made great progress due to the use of smart materials such as piezoelectric materials, optical fibers and shape memory alloys allowing the development of miniaturized systems with greater resolution, analysis speed and reliability. One of the techniques that emerged was the electromechanical impedance (EMI) or electromechanical admittance (EMA) technique. This technique is based on piezoelectric materials such as the Lead Zirconate Titanate (PZT) patches. A PZT is a transducer that transduces electrical energy to mechanical and vice versa due to the electromechanical coupling of these materials. A PZT produces electrical charge when it is subjected to a strain field and conversely produces mechanical strain when an electric field is applied. The technique uses the admittance or impedance spectrum signatures acquired across the electrodes of a PZT patch bonded to a host structure. The approach is based on the relation existing between the PZT's electrical impedance and the structural mechanical impedance of the host structure which is affected by the existence of damage. So typically the PZT patch is subjected to an alternate voltage excitation from an impedance analyzer sweeping through a particular frequency range. The patch actuates the host structure and structural response is sensed and measured in terms of the electromechanical impedance or admittance of the patch. Any deviation from the baseline undamaged spectrum is an indication of damage.

The EMI technique is capable of diagnosing a wide range of structures and materials. Applications can be found for reinforced concrete, pipeline structures, engine components etc. Bhalla et al. [Bhalla and Soh (2004)] solved the equations for surface bonded PZT. The applications of the EMI technique in concrete structures are abundant. Soh et al. [Soh, Tseng, Bhalla et al. (2000)] carried out a destructive load test of a reinforced concrete prototype bridge. Tseng et al. [Tseng and Wang (2004)] caused artificial damage in a concrete beam and performed both experimental and numerical study on damage detection. Park et al. [Park, Ahmad, Yun et al. (2006)] also investigated

multiple crack damage of concrete beam, both numerical and experimental. Lim et al. [Lim, Bhalla and Soh (2006)] applied the EMI technique to detect damage of an aluminum truss, an aluminum beam and a concrete cube. Song et al. [Song, Gu, Mo et al. (2007)] used embedded PZTs to detect damage on a reinforced, full size bent cap. Yang et al. [Yang, Hu and Lu (2008)] used structural mechanical impedance (SMI) extracted from the electromechanical impedance of a PZT for damage detection and compared SMI to the EMI technique. The experimental procedure included a two storey concrete frame and damage was inducted via a shake table. Yang et al. [Yang and Divsholi (2010)] proposed a sub-frequency approach for localization of damage in concrete structures. They used, like most of the previously mentioned researchers, the RMSD damage index. Na and Lee [Na and Lee (2012)] investigated artificial damage induced by circular saw on concrete specimens. Wang et al. [Wang, Song and Zhu (2013)] performed an experimental and numerical study of damage detection on a concrete beam using the correlation coefficient (CC) as damage index. All the above applications refer to damage detection in concrete structures.

Another field of interest since late 00's was the monitoring of strength gain of concrete. At the same period interest arose for the creation of an on line SHM system. Tawie et al. [Tawie and Lee (2010)] monitored the strength gain of concrete using surface bonded PZT and using RMSD, MAPD (Mean Absolute Percentage Deviation) and CC (Correlation Coefficient) as damage indices. Yang et al. [Yang, Divsholi and Soh (2010)] proposed a reusable PZT to monitor strength gain. Annamdas et al. [Annamdas, Yang and Soh (2010)] monitored the strength gain using embedded PZT sensors to improve the wave propagation in the mass of concrete. Providakis et al. [Providakis and Liarakos (2011)] proposed a wireless miniaturized impedance measuring system (Wireless Teflon-based integratEd monitoring sYstEm or T-WiEYE) for early age strength gain of concrete. Tawie et al. [Tawie and Lee (2011)] proposed a reusable PZT sensor packaging for strength gain of concrete. The cubic concrete specimens were also used in cyclic compressive test and the packaged sensor was recovered. Quinn et al. [Quinn, Kelly and Barrett (2012)] also monitored the curing process of concrete and later used them for compression test. They also proposed a remote measuring system based on AD 5933 Analog Devices chip. Providakis et al. [Providakis, Liarakos and Kampianakis (2013)] proposed a remote wireless early age monitoring system and a sensor packaging rendering the sensor reusable. Cortez et al. [Cortez, Filho and Baptista (2013)] proposed a microcontroller measuring not the impedance across the electrodes of a PZT itself but the variations of output voltage, which was tested on an aluminum beam. Providakis et al [Providakis, Tsistrakis, Voutetaki et al. (2015, 2016)] proposed a low cost wireless prototype system (WIAMS-Wireless Impedance or Admittance Monitoring System) which does not measure impedance itself but the output voltage across the electrodes of a PZT. The system was tested for damage detection in cubic concrete specimens under uniaxial compressive load and bending test of lightly reinforced concrete beams to detect shear failure. The study also used 2-D error statistics for the quantification of damage [Providakis, Tsistrakis, Voutetaki et al. (2015)] and extreme value statistics [Providakis, Tsistrakis, Voutetaki et al. (2016)].

Another NDE technique used in a number of applications, especially when minimum contact conditions are required is the Laser Doppler Vibrometry (LDV). The LDV

technique is a remote and non-contact method to measure the velocity of a specific point on a vibrating structure alongside the direction of the beam. The scanning version of the LDV (SLDV) measures point-by-point surface velocities using interferometric techniques and galvanometric driven mirrors steering the laser beam. The ability to direct the laser beam at a grid of desired points and quickly perform a series of velocity measurements allows the creation of color maps of velocities. The Scanning Laser Doppler Vibrometer (SLDV) has been used in applications where minimum or no contact with the structure under test is allowed. Typically points with higher oscillation velocity show indication of possible detachment or damage in the vicinity of that specific point. The excitation methods vary depending on the special needs of each study. Typically ambient noise or acoustic waves are used as excitation methods, especially in applications where no contact is allowed.

Specifically Castellini [Castellini (2000)] performed damage detection using standard loudspeakers, constant directivity loudspeakers, elliptic acoustic mirror and piezoelectric actuators as excitation method on fresco, icon and composite samples. Castellini et al. [Castellini, Esposito, Marchetti et al. (2003)] performed damage detection on mosaics, ceramics, inlaid wood and easel paintings using PZT actuators and horn loudspeakers. Esposito et al. [Esposito, Copparoni and Naticchia (1998)] proposed a non-invasive diagnostic on buildings of special interest using SLDV measurements. Herdier et al [Herdier, Jenkins, Dogheche et al. (2006)] used SLDV for evaluating the piezoelectric coefficient  $d_{33}$  on piezoelectric MEMS. Siringoringo et al. [Siringoringo and Fujino (2006)] applied SLDV on a steel plate to detect damage using ambient noise as excitation method. Fukushima et al. [Fukushima, Nishizawa and Sato (2009)] used the SLDV for measuring waveforms created from piezoelectric transducers. Lee et al. [Lee and Iijima (2010)] used SLDV to measure high frequency piezoelectric displacement of PZT films. Collini [Collini (2011)] presented a contactless technique for health monitoring of ancient frescoes based on SLDV. Yu et al. [Yu and Tian (2013)] proposed a hybrid PZT and SLDV approach using lamb waves for structural health monitoring.

In the present study the applicability of a combination of the two methods described above is investigated, as well as the application of damage index denoted as ECAR (Ellipse to Circle Area Ratio) based on 2-D error statistics. Damage index ECAR will be presented in length at a later chapter. In typical EMI technique the electrical properties of a PZT were measured via an impedance analyzer and any change in the electrical properties of the PZT indicated a change in the mechanical properties of the host structure due to electro-mechanical coupling of the PZT. Since all the conditions except from the mechanical properties of the host structure remain the same, any change is an indication of the existence of damage in the host structure. In the proposed technique the excitation of the PZT patches is made using a function generator. Due to the bonding of the PZTs with the structure under test (SUT), the SUT is actuated due to the electrical excitation of the PZTs. The response of the PZT-Host structure is obtained using the SLDV by measuring the oscillation velocity of the bonded PZT patches parallel to the laser beam. Velocity-frequency spectrums can be obtained and, like in typical EMI technique, changes in the spectrum indicate the existence of damage in the vicinity of the specific PZT patch where the alterations compared to the undamaged state is observed.

The application of the proposed method that combines the EMI technique and Scanning Laser Doppler Vibrometry provides a number of advantages compared to the application of each one separately. It is a remote, but not non-contact contrary to the classic SLDV, technique that provides the ability of simultaneous scan of large scale structures by connecting the PZTs with the function generator in parallel and getting a separate velocity-frequency plot for each PZT patch. The same result using the traditional EMI technique would require the same number of impedance analyzers as the number of PZTs attached to the SUT. Connecting the PZTs in parallel with one impedance analyzer would provide only one spectrum for the sum of the PZTs. So even if a change in a single PZT is not “drowned”, the localization of the damage would be impossible. The excitation of the PZTs using a function generator allows the actuation of the PZTs with alternate current of up to 20 Volts and using an amplifier even 10 fold up, up to 200 Volts. Commercial impedance analyzers can actuate up to 1-2 Volts, depending the model, without the possibility of connection with an amplifier. The greater amplitude of excitation results in larger amounts of energy that can be induced to the host structure and thus a larger sensing region. The limited sensing area in a highly dispersive material such as concrete is one of the greater drawbacks of the EMI technique. Additionally the greater disadvantage of SLDV is the inability to scan ragged surfaces due to the scattering of the reflected beam. Using the PZTs as scanning points takes advantage of the high reflectability of the surface of the PZT. Additionally scanning a large scale structure is realized far more quickly (in few seconds, depending the number of scan points) and more accurately (6337 values in 64 msec using the SLDV, compared to 200-400 values in 3-5 min depending on the model). Finally using the SLDV software the measurements are taken directly in the frequency domain contrary to an oscilloscope where the measurements are obtained in the time domain.

## 2 The ECAR damage index

The probability density function (PDF) of a continuous random variable gives the relative likelihood of any outcome in a continuum occurring. In other words, it is used to specify the probability of a random value to fall within a particular range of values. For the scalar case, the PDF of a random variable  $x$  normally distributed with mean value  $\mu$  and variance  $\sigma^2$  is [Ribeiro (2004)]:

$$f(x) = \frac{1}{\sqrt{2\pi}\cdot\sigma} \exp\left[-\frac{(x-\mu)^2}{2\sigma^2}\right], -\infty < x < \infty \quad (1)$$

In this case the PDF is bell shaped and symmetrical around the mean value  $\mu$ . The mean value and the variance  $\sigma^2$  are the two parameters that can completely characterize a normally distributed random variable. A useful evaluation of the PDF is the locus of the points where PDF is greater or equal to a specific value  $K$ . For the scalar case the locus is a line segment (Fig. 1).

In our case we deal with normal random vectors and more specifically with two dimension normal random vectors. We denote the velocity measurements obtained in the undamaged state as  $X$  and the measurements obtained for a damaged state as  $Y$ . The pair of  $X$  and  $Y$  are measurements are considered as normal random variables, so the vector  $Z$  can be considered as a 2-D normal random vector.

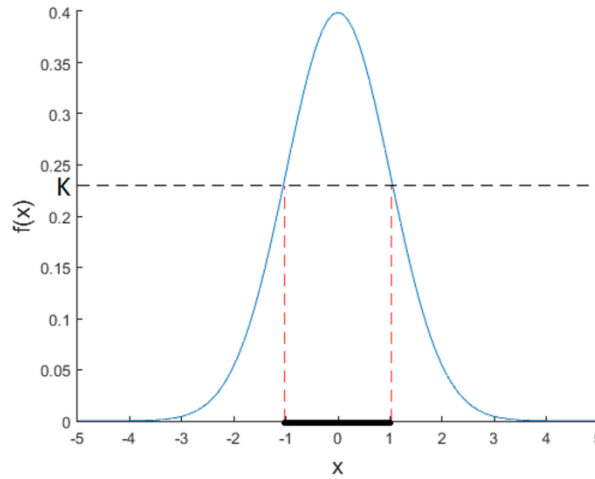


**Figure 1:** Locus of points where PDF is greater than K

$$Z = \begin{bmatrix} X \\ Y \end{bmatrix} \tag{2}$$

The mean of vector Z is defined as E(Z):

$$E[Z] = E \begin{bmatrix} X \\ Y \end{bmatrix} = \begin{bmatrix} m_X \\ m_Y \end{bmatrix} \tag{3}$$

where  $m_X$  is the mean vector of random variable X and  $m_Y$ , the mean vector of random variable Y. The covariance matrix is defined as  $\Sigma$ . The matrix  $\Sigma$  is symmetric.

$$\Sigma = \begin{bmatrix} E(X - m_X)^2 & E(X - m_X)(Y - m_Y) \\ E(X - m_X)(Y - m_Y) & E(Y - m_Y)^2 \end{bmatrix} = \begin{bmatrix} \sigma_X^2 & \sigma_{XY} \\ \sigma_{XY} & \sigma_Y^2 \end{bmatrix} \tag{4}$$

where  $\sigma_X^2$  and  $\sigma_Y^2$  are the variances for random variables X and Y respectively and  $\sigma_{XY}$  is the covariance of X and Y.

The PDF for the random normal vector Z is [Ribeiro (2004)]:

$$f(Z) = \frac{1}{2\pi\sqrt{\det\Sigma}} \exp \left[ -\frac{1}{2} [X - m_X \ Y - m_Y] \Sigma^{-1} [X - m_X \ Y - m_Y]^T \right] \tag{5}$$

Like in the scalar case mentioned above, a useful evaluation is the locus of points where PDF is greater or equal to a specific value,  $K_1$ . For this second order case the locus is an ellipse, given by Ribeiro [Ribeiro (2004)]:

$$\left\{ (x, y): \frac{1}{2\pi\sqrt{\det\Sigma}} \exp \left[ -\frac{1}{2} [x - m_X \ y - m_Y] \Sigma^{-1} [x - m_X \ y - m_Y]^T \right] \geq K_1 \right\} \tag{6}$$

which is equivalent to:

$$\left\{ (x, y): \left[ [x - m_X \ y - m_Y] \Sigma^{-1} \begin{bmatrix} x - m_X \\ y - m_Y \end{bmatrix} \right] \leq K \right\}, \text{ with } K = -2 \ln \left( 2\pi K_1 \sqrt{\det(\Sigma)} \right) \tag{7}$$

In all cases the center of the ellipse is  $(m_X, m_Y)$ . Depending on the value of the correlation coefficient the axes of the ellipse are either parallel to x and y coordinates or rotated around its origin by an angle. The correlation coefficient is defined as:

$$\rho = \frac{\sigma_{XY}}{\sigma_X \sigma_Y} \tag{8}$$

and the covariance matrix can be expressed as:

$$\Sigma = \begin{bmatrix} \sigma_X^2 & \rho\sigma_X\sigma_Y \\ \rho\sigma_X\sigma_Y & \sigma_Y^2 \end{bmatrix} \tag{9}$$

When  $\rho=0$  the axes of the ellipse are parallel to x and y coordinates while when  $\rho \neq 0$  they are rotated around an angle. Specifically, when  $\rho=0$  the covariance matrix is diagonal and the eigenvalues  $\lambda_1=\sigma_x^2$  and  $\lambda_2=\sigma_y^2$ . So the locus can be expressed as:

$$\left\{ (x, y): \frac{(x-m_X)^2}{\sigma_X^2} + \frac{(y-m_Y)^2}{\sigma_Y^2} \leq K \right\} \text{ or } \left\{ (x, y): \frac{(x-m_X)^2}{K \cdot \sigma_X^2} + \frac{(y-m_Y)^2}{K \cdot \sigma_Y^2} \leq 1 \right\} \tag{10}$$

which is an ellipse centered at  $(m_X, m_Y)$  and two axes with lengths  $2\sigma_X\sqrt{K}$  and  $2\sigma_Y\sqrt{K}$  for x and y respectively.

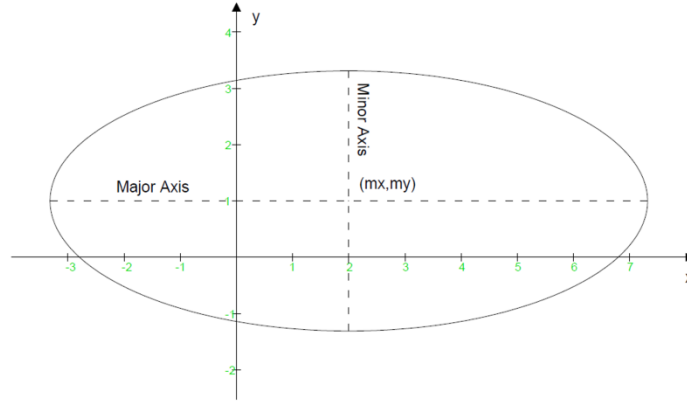


**Figure 2:** Locus of constant PDF with  $\rho=0$ , i.e. axis parallel to coordinate frame

In cases where the data is not uncorrelated, such that  $\rho \neq 0$ , the resulting error ellipse will not be axis aligned. So whereas in the first case the calculated the variances  $\sigma_X$  and  $\sigma_Y$  parallel to the x-axis and y-axis, we now need to calculate these variances parallel to what will become the major and minor axis of the confidence ellipse. These directions are actually the directions in which the data varies the most, and are defined by the covariance matrix. The covariance matrix can be considered as a matrix that linearly transformed some original data to obtain the currently observed data. The direction vectors along such a linear transformation are the eigenvectors of the transformation matrix. The eigenvalues therefore represent the spread of the data in the direction of the eigenvectors. In the case of axis aligned error ellipses, i.e. when the covariance equals zero, the eigenvalues equal the variances of the covariance matrix and the eigenvectors are equal to the definition of the x-axis and y-axis. In the case of arbitrary correlated data, the eigenvectors represent the direction of the largest spread of the data, whereas the eigenvalues define how large this spread really is. So to obtain the orientation of the error ellipse we calculate the angle of the largest eigenvector with the x axis. So similarly to the axis aligned case, the confidence ellipse can be defined with the major axis  $2\sqrt{\lambda_1 K}$

and a minor axis  $2\sqrt{\lambda_2 K}$ , with  $\lambda_1$  and  $\lambda_2$  representing the eigenvalues of  $\Sigma$ . So the locus can be expressed as [Ribeiro (2004)]:

$$\left\{ (w_1, w_2): \frac{w_1^2}{K \cdot \lambda_1} + \frac{w_2^2}{K \cdot \lambda_2} \leq 1 \right\} \quad (11)$$

where the new coordinates system is defined by  $w_1$  and  $w_2$ , and the orientation of the confidence ellipse can be found by:

$a = \tan^{-1} \frac{V_1(y)}{V_1(x)}$ , where  $V_1$  is the eigenvector of the covariance matrix that corresponds to the largest eigenvalue or:

$$a = \frac{1}{2} \tan^{-1} \left( \frac{2\rho\sigma_X\sigma_Y}{\sigma_X^2 - \sigma_Y^2} \right), \text{ for } -\frac{\pi}{4} \leq a \leq \frac{\pi}{4} \text{ and } \sigma_X \neq \sigma_Y \quad (12)$$

So the length of the axis of the ellipse and the angle they form with the x y coordinates are function of the constant  $K_1$ , the eigenvalues of  $\Sigma$  and the correlation coefficient. The constant  $K_1$  is obtained from the chi square distribution for the desired confidence level (cumulative probability) and the existing degrees of freedom which in our case is 2. For example for 2 degrees of freedom and for a confidence level of 50%, the chi square critical value is 1.39. In the present study, in all cases the confidence level was 99.5% and the critical value was 10.6.

In the special case when the eigenvalues are equal, which occurs when  $\sigma_X = \sigma_Y$ , the ellipse degenerates into circle, of the same confidence level, as the two foci coincide.

So the damage index denoted as ECAR (Ellipse to Circle Area Ratio) [Providakis, Tsistrakis, Voutetaki et al. (2015)] is based on the ratio of the area of the ellipse for a specific confidence level to the area of the circle of the same confidence level.

$$ECAR = \frac{\text{Area of a confidence ellipse of a given probability}}{\text{Area of the confidence circle for the same probability and confidence level}} \quad (13)$$

ECAR index has the benefit that could directly characterize the degree of divergence existed between the healthy baseline and any current structural integrity condition since the divergence between the area of confidence ellipse of interest and the confidence circle of equivalent probability increases as the ellipse becomes thinner and more elongated, which is exactly the case where current structural integrity condition is very close to the healthy one, which, equivalently in turn, could be considered as an indicator of no damage case.

Except from the proposed damage index described above, the Root Mean Square Deviation (RMSD) damage index is also used in this paper as the damage index most commonly used in similar applications. It is therefore used as a reference for the ECAR damage index. RMSD is defined as:

$$RMSD(\%) = \sqrt{\frac{\sum_{i=1}^N (v_i^1 - v_i^0)^2}{\sum_{i=1}^N (v_i^0)^2}} \quad (14)$$

Where:  $v_i^1$  is the post damage surface velocity of the PZT for the  $i^{\text{th}}$  frequency  $v_i^0$  is the baseline (pre-damage) surface velocity of the PZT for the  $i^{\text{th}}$  frequency.

### **3 Experimental setup and procedure**

Three sets of experiments were carried out as proof of concept of the described methodology and damage index. In all three of them the excitation of the PZTs is done via a function generator using a chirp signal with duration time of 60 msec, the interval between two chirp signals was 4 msec and the scanning frequencies were 1 to 100 kHz. The response measurements were obtained using a PSV 500H Scanning Laser Doppler Vibrometer of Polytec. The measurements were obtained in frequency domain, as the PSV 500H software uses a Fast Fourier Transform (FFT), with a sampling time of 64 msec and 6400 number of FFT lines.



**Figure 3:** Compression test experimental setup. The PSV 500H Scanning Laser Doppler Vibrometer consisting of the scanning head and the control unit aiming at concrete specimen placed on the compression machine

#### **3.1 Compression tests**

The first set of experiments was cyclic compressive uniaxial test of cubic  $150 \times 150 \times 150$  mm concrete specimens made by a mixing proportion of 1:0.62:2.55:3.83 ratio by mean of cement (cement: water: fine aggregate: Coarse aggregate). Each specimen was equipped with a PIC 255 PZT attached on its surface and was subjected to different, ascending uniaxial compressive loads until failure. The specimens are denoted as C1 to C3. In specimen C1 PZT was attached with hard two component adhesive glue. In order to investigate the possibility of applying the aforementioned technique in structures with a sensitive surface or structures where the possibility of permanent attachment of the PZT is not an option, the attachment of PZTs in specimens C2 and C3 was made using a double sided adhesive tape. The first set of measurements was taken prior to any load being subjected to the specimen under test and was the baseline measurement. The following measurements cyclic ascending compressive loads with the measurements being obtained at the end of each cycle.

The measurement results for each case are considered random vectors sized  $[6337 \times 1]$ . The ellipse and circle areas for 99.5% probability were obtained using Matlab 15 [Mathworks (2015)]. The confidence circle radius was obtained using the Confidence Region Radius (CRR) function of Matlab [Mathworks (2015)] for probability 99.5% of the covariance matrix of the baseline measurement compared to each load case.

3.1.1 Specimen C1

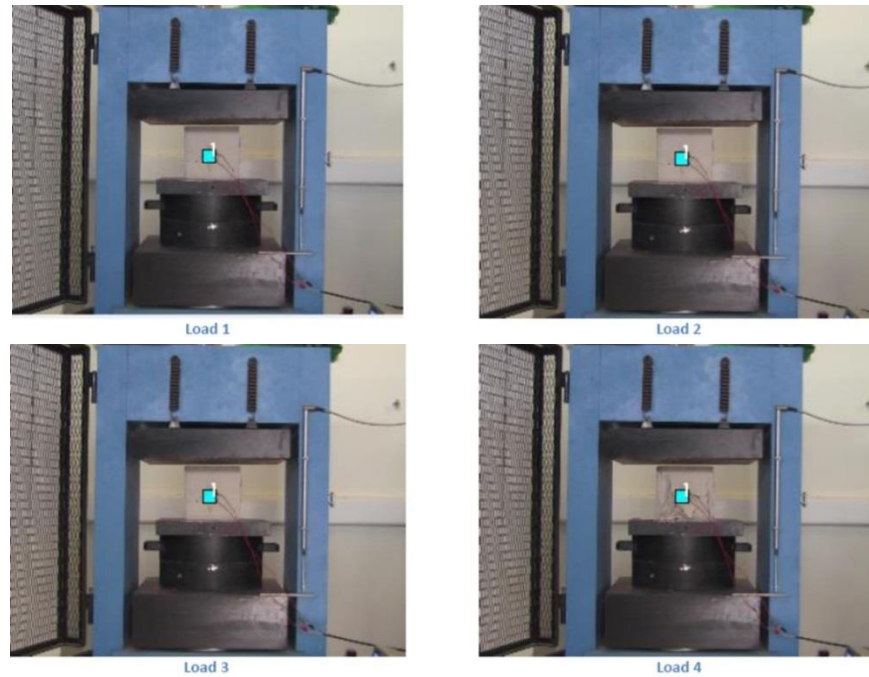


**Figure 4:** Experimental setup for compression test and the cubic concrete specimen at the end of each cycle

The covariance matrices were also calculated via Matlab 15 and are presented in Tab. 1. The velocity spectrums and the RMSD and ECAR damage indices are shown in Fig. 5.

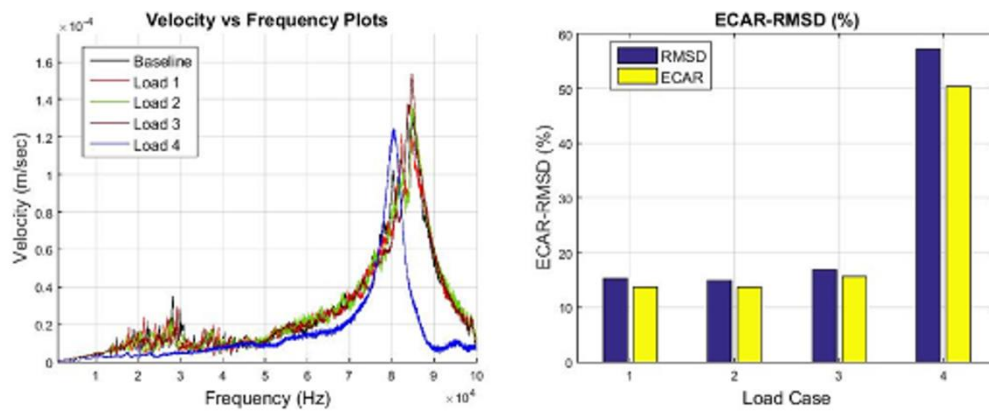


**Figure 5:** Velocity spectrum (left) and damage indices (right) for load cases 1-4

**Table 1:** Covariance matrices of baseline and each load case

Baseline-Load 1	$\Sigma_1 = \begin{bmatrix} 8.082e-10 & 7.405e-10 \\ 7.405e-10 & 7.074e-10 \end{bmatrix}$
Baseline-Load 2	$\Sigma_2 = \begin{bmatrix} 8.082e-10 & 7.606e-10 \\ 7.606e-10 & 7.462e-10 \end{bmatrix}$
Baseline-Load 3	$\Sigma_3 = \begin{bmatrix} 8.082e-10 & 7.883e-10 \\ 7.883e-10 & 7.074e-10 \end{bmatrix}$
Baseline-Load 4	$\Sigma_4 = \begin{bmatrix} 8.082e-10 & 7.405e-10 \\ 7.405e-10 & 8.114e-10 \end{bmatrix}$

The eigenvalues, eigenvectors and rotation angle for each case are shown in Tab. 2:

**Table 2:** The eigenvalues, eigenvectors and rotation angle for each load case

Load Case	Eigenvectors	Eigenvalues	Rotation angle (°)
Baseline-Load 1	$\begin{bmatrix} 0.6827 & -0.7307 \\ -0.7307 & -0.6827 \end{bmatrix}$	$\begin{bmatrix} 1.5549e-11 & 0 \\ 0 & 1.5001e-9 \end{bmatrix}$	223.05
Baseline-Load 2	$\begin{bmatrix} 0.6926 & -0.7214 \\ -0.7214 & -0.6926 \end{bmatrix}$	$\begin{bmatrix} 1.5547e-11 & 0 \\ 0 & 1.5385e-9 \end{bmatrix}$	223.83
Baseline-Load 3	$\begin{bmatrix} -0.7078 & 0.7064 \\ 0.7064 & 0.7078 \end{bmatrix}$	$\begin{bmatrix} 2.1505e-11 & 0 \\ 0 & 1.5981e-9 \end{bmatrix}$	45.06
Baseline-Load 4	$\begin{bmatrix} 0.5942 & -0.8043 \\ -0.8043 & -0.5942 \end{bmatrix}$	$\begin{bmatrix} 1.6925e-11 & 0 \\ 0 & 1.1570e-9 \end{bmatrix}$	216.46

The radius of the confidence circle, its area, the ellipse area for 99.5% confidence level and the ECAR damage index (Ellipse Area/Circle Area) are shown in the table below:

**Table 3:** The radius of the confidence circle, its area, the ellipse area for 99.5% confidence level and the ECAR damage index for each load case

Load Case	Circle Radius	Circle Area	Ellipse Area	ECAR (%)
Baseline-Load 1	1.09E-04	3.72E-08	5.08E-09	13.66
Baseline-Load 2	1.10E-04	3.81E-08	5.21E-09	13.66
Baseline-Load 3	1.12E-04	3.96E-08	6.17E-09	15.56
Baseline-Load 4	9.64E-05	2.92E-08	1.47E-08	50.38

**Table 4:** Damage indices values

	Load 1	Load 2	Load 3	Load 4
	221.5 (kN)	305.7 (kN)	413.2 (kN)	677.4 (kN)
<b>RMSD (%)</b>	15.20	14.83	16.92	57.31
<b>ECAR (%)</b>	13.66	13.66	15.56	50.38

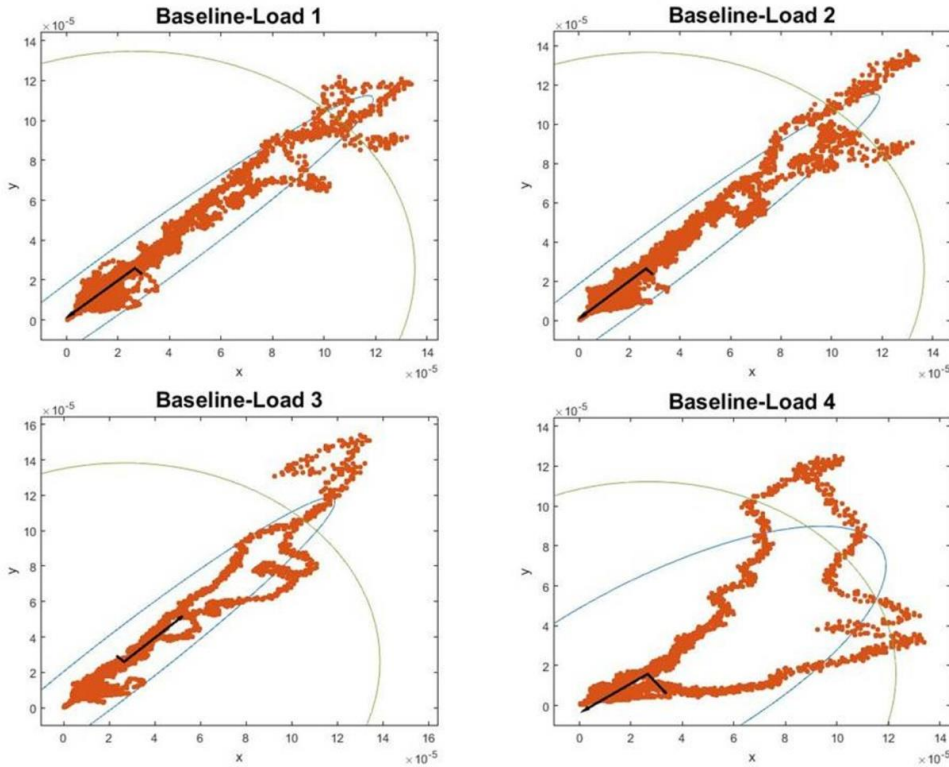


**Figure 6:** Error ellipse and error circle plots for 99.5% confidence level for Loads 1-4

As described in previous chapter, for early load levels with less damage and therefore less difference compared to the baseline measurements, the ellipse is thinner and more elongated and the area of the ellipse is therefore smaller. In this case the majority of the measurement values are located along the axis of the largest eigenvector and the in the special case when there is no difference between the baseline and the investigated load case the ellipse degenerates to a line with the ECAR value taking the extreme value 0. In Fig. 6 the eigenvectors are shown in black color. The orientation of the ellipse is obvious and the rotation angle mentioned in Tab. 2 is the angle between the largest eigenvector and the x axis. As the damage grows bigger thus the differences in the values grow bigger resulting in a greater dispersion of the values on the plot and bigger area of the ellipse. As mentioned in the previous chapter the eigenvalues represent the spread of the data in the direction of the eigenvectors. In the special case of equal eigenvalues the dispersion of values is the same in both directions which means that the ellipse degenerates to a circle

as the two foci of the ellipse coincide. In this case the ECAR index takes the extreme value 1 which is the upper limit of the index. The differences between the load cases and all the values calculated via Matlab are represented in Fig. 6.

The following experiments will be presented briefly as the calculating procedure is exactly the same as presented for compression for Specimen 1.

3.1.2 Specimen C2

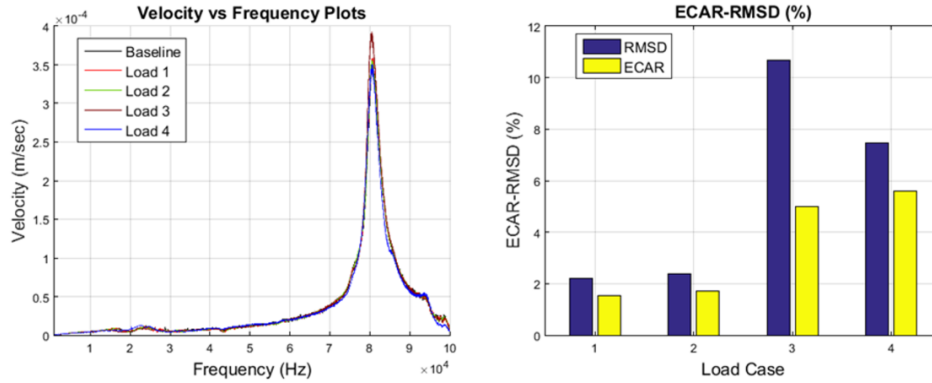


Figure 7: Velocity spectrum (left) and damage indices (right) for load cases 1-4

Table 5: Damage indices values

	Load 1	Load 2	Load 3	Load 4
	224.6 (kN)	407.6 (kN)	618.4 (kN)	595.4 (kN)
<b>RMSD (%)</b>	2.18	2.39	10.66	7.48
<b>ECAR (%)</b>	1.53	1.72	5.00	5.59

3.1.3 Specimen C3

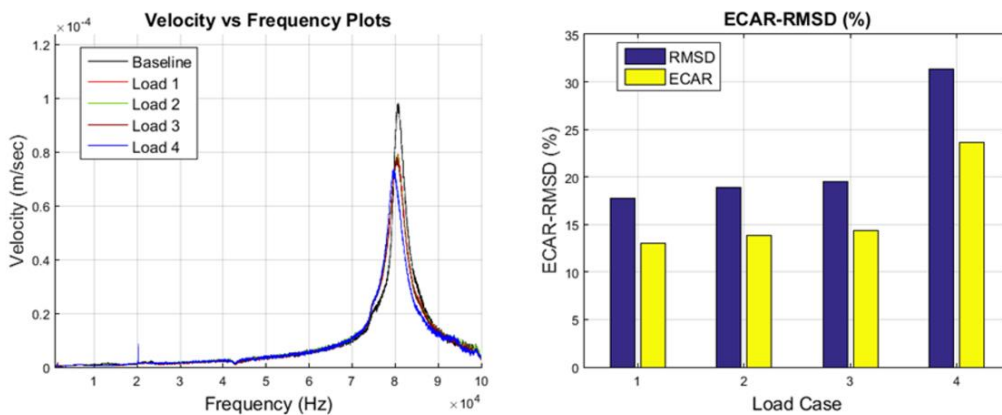


Figure 8: Velocity spectrum (left) and damage indices (right) for load cases 1-4

**Table 6:** Damage indices values

	<b>Load 1</b>	<b>Load 2</b>	<b>Load 3</b>	<b>Load 4</b>
	<b>224.6 (kN)</b>	<b>407.6 (kN)</b>	<b>618.4 (kN)</b>	<b>595.4 (kN)</b>
<b>RMSD (%)</b>	17.73	18.88	19.55	31.38
<b>ECAR (%)</b>	13.01	13.84	14.33	23.59

### 3.2 Three point bending tests

The second set of experiments that was carried out was bending test of lightly reinforced concrete beams, sized  $100 \times 150 \times 750$  mm, of the same mixing proportions as in the first set of experiments and reinforced with one steel rod with 10 mm diameter. As in the first set of experiments, the loading pattern was ascending until failure, with the measurements being made in the unloaded state. The specimens are denoted as B1 to B6. All the beams were lightly reinforced with one longitudinal steel rod of 10 mm diameter and equipped with two PZTs, located in the vicinity of the two possible shear failure routes. The objective of the experiment was to detect the shear failure due to vertical force. Due to low cohesion between the steel rod and concrete, specimens B2, B3 and B4 failed due to bending moment as shown in the following figures. Even though the specific specimens did not fail in the predicted way, they are still included in this article as the intensity and the location of the damage was successfully detected.

The PZTs in specimen B1 were attached using hard two component adhesive glue while in the rest using a double sided adhesive tape.

#### 3.2.1 Specimen B1



**Figure 9:** Experimental set up for bending test



**Figure 10:** Shear failure pattern (Failure in the right side shear diagonal)

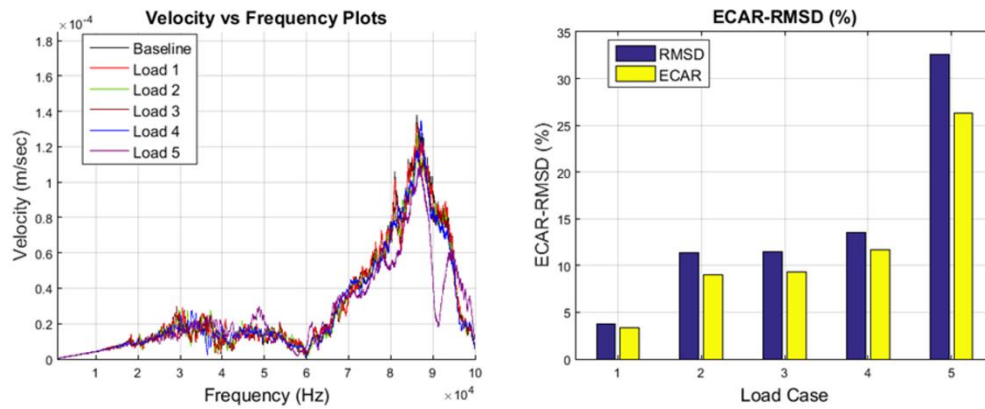


**Figure 11:** Velocity spectrum and damage indices for load cases 1-5 of the left PZT

**Table 7:** Damage indices values

	PZT RIGHT		PZT LEFT	
	ECAR (%)	RMSD (%)	ECAR (%)	RMSD (%)
<b>Load 1</b>	3.31	3.75	2.98	5.29
<b>Load 2</b>	9.05	11.32	9.46	11.73
<b>Load 3</b>	9.28	11.47	9.69	12.03
<b>Load 4</b>	11.64	13.51	12.66	14.54
<b>Load 5</b>	26.29	32.58	17.70	20.29

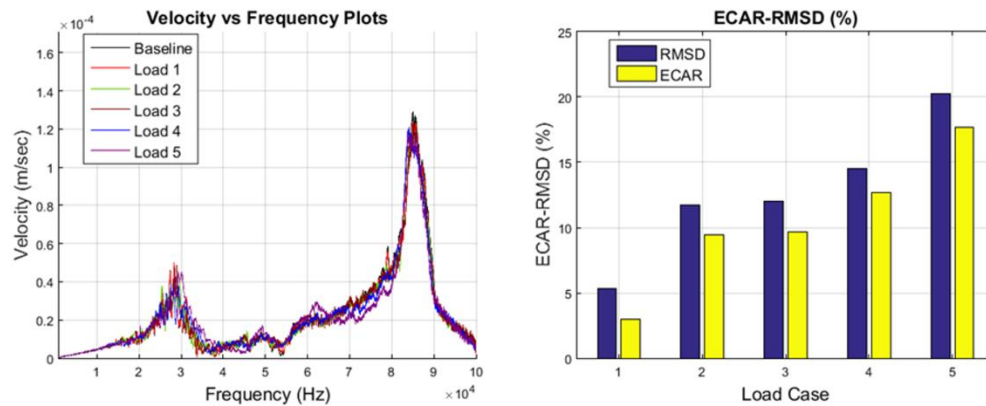


**Figure 12:** Velocity spectrum and damage indices for load cases 1-5 of the right PZT

### 3.2.2 Specimen B2

As shown in Fig. 13 the major failure occurred in the left side of the beam which was successfully detected by the indices. Due to the light reinforcement of the beam damage also occurred in the vicinity of the right PZT which occurred earlier in load case 3, explaining the spike in damage indices for the right PZT.



**Figure 13:** Failure pattern of B2

**Table 8:** Damage indices values

	PZT LEFT		PZT RIGHT	
	ECAR (%)	ECAR (%)	ECAR (%)	RMSD (%)
<b>Load 1</b>	1.84	2.74	0.79	1.01
<b>Load 2</b>	2.58	4.05	2.87	5.51
<b>Load 3</b>	6.90	10.83	17.44	30.12
<b>Load 4</b>	23.44	63.23	18.41	46.04

### 3.2.3 Specimen B3

As in beam specimen B2, due to light bending reinforcement of the beam a big “tooth” shaped piece of concrete was detached as shown in Fig. 14 resulting in a big spike in both sensors damage indices, making the results inconclusive as far as the detection of the shear failure is concerned.



**Figure 14:** Failure pattern of B3

**Table 9:** Damage indices values

	PZT RIGHT		PZT LEFT	
	ECAR (%)	ECAR (%)	ECAR (%)	RMSD (%)
<b>Load 1</b>	3.82	5.23	1.96	2.63
<b>Load 2</b>	3.09	3.73	2.09	3.02
<b>Load 3</b>	3.25	3.96	2.55	3.81
<b>Load 4</b>	28.28	47.86	36.94	49.89

### 3.2.4 Specimen B4

Damage occurred near both PZTs (Fig. 15) with the damage occurring in the left side being more severe as is obvious after evaluating the damage indices.



**Figure 15:** Failure pattern of B4

**Table 10:** Damage indices values

	<b>PZT LEFT</b>		<b>PZT RIGHT</b>	
	<b>ECAR (%)</b>	<b>ECAR (%)</b>	<b>ECAR (%)</b>	<b>RMSD (%)</b>
<b>Load 1</b>	2.46	3.07	3.71	5.50
<b>Load 2</b>	1.67	2.11	2.69	3.59
<b>Load 3</b>	1.93	2.41	3.54	5.04
<b>Load 4</b>	32.46	39.94	17.14	21.85

### 3.2.5 Specimen B5

Damage detection along the right hand side shear diagonal was successful in beam specimen B5.

**Figure 16:** Failure pattern of B5**Table 11:** Damage indices values

	<b>PZT LEFT</b>		<b>PZT RIGHT</b>	
	<b>ECAR (%)</b>	<b>ECAR (%)</b>	<b>ECAR (%)</b>	<b>RMSD (%)</b>
<b>Load 1</b>	4.68	5.69	5.20	6.50
<b>Load 2</b>	5.73	6.95	6.55	8.11
<b>Load 3</b>	5.70	6.99	8.85	10.86
<b>Load 4</b>	6.68	8.83	20.94	25.54

**Table 12:** Damage indices values

	<b>PZT LEFT</b>		<b>PZT RIGHT</b>	
	<b>ECAR (%)</b>	<b>ECAR (%)</b>	<b>ECAR (%)</b>	<b>RMSD (%)</b>
<b>Load 1</b>	1.53	1.87	1.38	1.98
<b>Load 2</b>	1.97	2.47	1.88	2.66
<b>Load 3</b>	2.91	3.54	3.07	8.51
<b>Load 4</b>	15.69	22.99	3.06	11.91

3.2.6 Specimen B6

Damage detection along the left hand side shear diagonal was successful in beam specimen B6. The bending test of the specific specimen underlines one of the greater shortcomings of the RMSD damage index. A spike in RMSD values is observed in the right PZT but not in the ECAR index. RMSD index can have a great fluctuation for great differences between few values. After evaluating the velocity plots (Fig. 18), it is obvious that the plots are similar and only have great difference in the peak value. The impact on the ECAR index in this case is slight while when using the RMSD index to detect damage we get a false alarm.



Figure 17: Failure pattern of B6

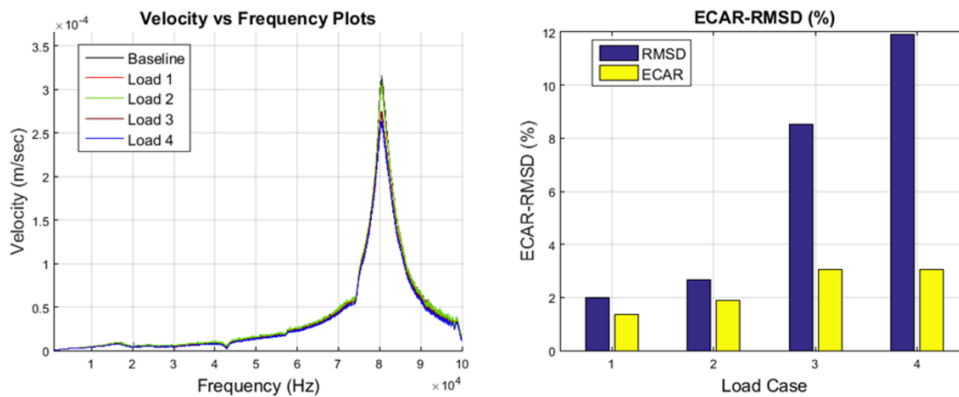


Figure 18: Velocity spectrum and damage indices for load cases 1-4 of the right PZT

3.3 Early age monitoring of concrete

The third set of experiments was the monitoring of the curing process of a cubic concrete specimen sized 150×150×150 mm of the same mixing proportion as in the first two sets of experiments. The PZT was attached using a two component adhesive glue on a hardened cement paste cube sized 50×50×50 mm that was manufactured prior to the casting of the concrete and its hydration process was finished. Therefore all the changes observed are due to changes in the concrete. The cement paste cube was then incorporated in the semi fluid fresh concrete during the casting. The particular choice was

made to enable the monitoring process to begin from the first critical hours after casting, even before the surface is hardened.

The monitoring process begun on the 15/12/2017 and the first measurement took place 2 hours after casting and was used as a reference value. The rest of the measurements were taken as shown in the table below.

**Table 13:** Damage indices for hours after casting the concrete compared to the baseline measurement

Hour	2	4	6	8	10	12	18	24	36	48	72
RMSD	0.00	89.57	93.64	100.76	102.01	103.00	48.10	74.44	79.03	81.45	58.95
ECAR	0.00	39.87	39.15	38.68	37.30	35.42	44.47	42.13	40.85	39.15	46.56
Hour	96	120	144	168	240	312	384	456	528	600	672
RMSD	62.36	78.27	83.26	98.44	77.68	81.39	73.61	71.75	71.87	87.18	67.82
ECAR	43.92	39.94	39.87	35.49	37.23	34.85	35.43	34.02	35.27	31.07	35.35

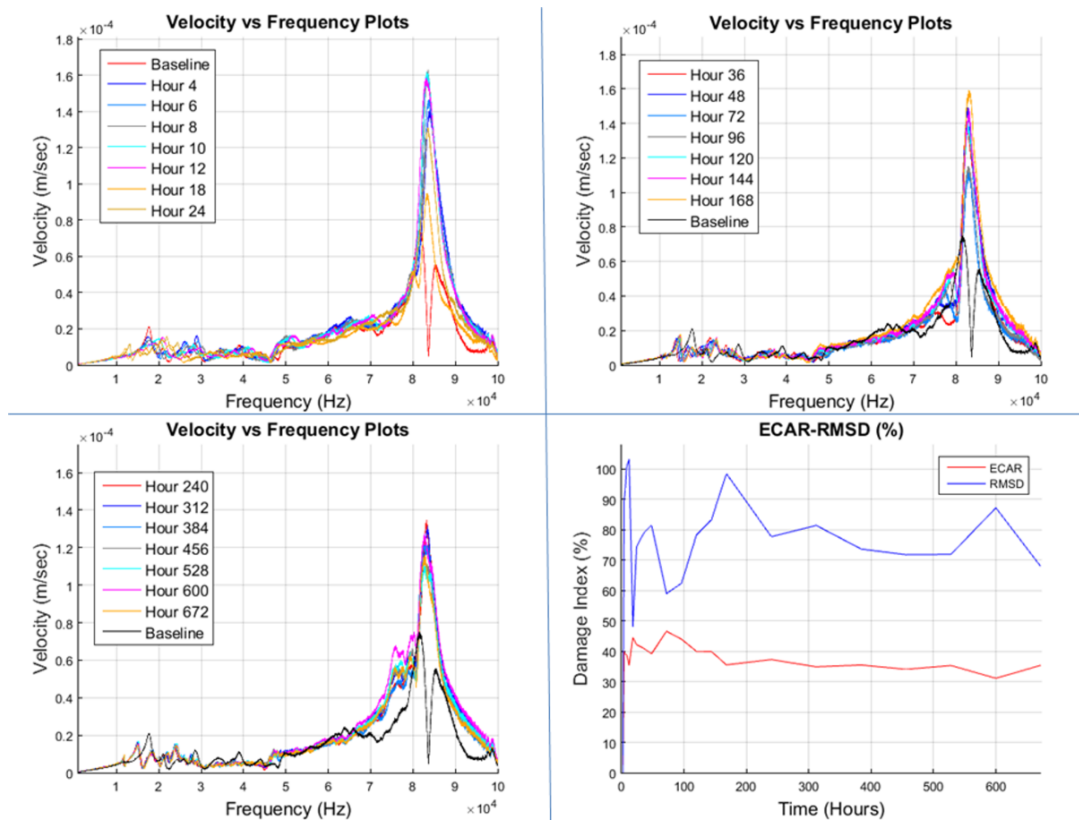


**Figure 19:** Velocity spectrums and damage indices

#### 4 Conclusions

This paper presents a new damage detection method using a combination of smart piezoelectric patches (PZT) and Scanning Laser Doppler Vibrometer in concrete

structures. The applicability of the proposed method and the use of the damage index denoted as ECAR are demonstrated through a number of experiments including cyclic ascending compressive test in cubic concrete specimens, cyclic ascending bending test of lightly reinforced concrete beams and strength gain monitoring of concrete. The proposed method was able to correlate the changes in the velocity spectrums of a PZT, obtained using a SLDV, with the existence of damage in the specimen under test. It was also demonstrated that the curing process of concrete can be monitored applying the same method. The use of the proposed damage index ECAR compared to RMSD damage index was also demonstrated especially in applications like strength gain monitoring where there is great difference compared to the initial measurements often leading in values greater than 100% when using RMSD.

**Acknowledgements:** The research work was supported by the Hellenic Foundation for Research and Innovation (HFRI) and the General Secretariat for Research and Technology (GSRT), under the HFRI PhD Fellowship grant 1444.

### References

- Annamdas, V. G. M.; Yang, Y.; Soh, C. K.** (2010): Impedance based Concrete Monitoring using Embedded PZT Sensors. *International Journal of Computational Civil and Structural Engineering*, vol. 1, no. 3, pp. 414-424.
- Bhalla, S.; Soh, C. K.** (2004): Structural health monitoring by piezo-impedance transducers. I: Modeling. *Journal of Aerospace Engineering*, vol. 17, no. 4, pp. 166.
- Castellini, P.** (2000): Non-invasive measurements of structural damage by laser scanning vibrometer: An experimental comparison among different exciters. *Shock and Vibration Digest*, vol. 3585.
- Castellini, P.; Esposito E.; Marchetti B.; Paone N.; Tomasini E.** (2003): New applications of Scanning Laser Doppler Vibrometry (SLDV) to non-destructive diagnostics of artworks: mosaics, ceramics, inlaid wood and easel painting. *Journal of Cultural Heritage*.
- Colla, C.; Gruner F.; Dieruff B.; Fiedler K.; Pascale G. et al.** (2010): SMOOHS (Smart Monitoring of Historic Structures). *Report D3.3: Sensor Development and Sensor Adaption (Part 2)*.
- Collini, L.** (2011): A non-destructive, contactless technique for the health monitoring of ancient frescoes. *Conference Proceedings of the Society for Experimental Mechanics Series*, vol. 3, pp. 867-874.
- Cortez, N. E.; Filho, J. V.; Baptista, F. G.** (2013): A new microcontrolled structural health monitoring system based on the electromechanical impedance principle. *Structural Health Monitoring*, vol. 12, no. 1.
- Doebling, S. W.; Farrar, C. R.; Prime, M. B.; Shevitz, D. W.** (1996): Damage identification and health monitoring of structural and mechanical systems from changes in their vibration characteristics: A literature review. *Los Alamos National Laboratory*, pp. 1-127.

**Esposito, E.; Copparoni, S.; Naticchia, B.** (1998): Recent progress in diagnostics of civil structures by laser vibrometry.

[http://www.artemis-srl.it/modules/referenze/Articolo\\_Canada.pdf](http://www.artemis-srl.it/modules/referenze/Articolo_Canada.pdf).

**Fukushima, Y.; Nishizawa, O.; Sato, H.** (2009): A performance study of a laser doppler vibrometer for measuring waveforms from piezoelectric transducers. *IEEE Transactions on Ultrasonics, Ferroelectrics, and Frequency Control*, vol. 56, no. 7.

**Herdier, R.; Jenkins, D.; Dogheche, E.; Rèmes, D.; Sulc, M.** (2006): Laser Doppler vibrometry for evaluating the piezoelectric coefficient d33 on thin film. *Review of Scientific Instruments*, vol. 77, no. 9.

**Jenkinson, A. F.** (1955): The frequency distribution of the annual maximum (or minimum) values of meteorological elements. *Quarterly Journal of the Royal Meteorological Society*, vol. 81, no. 348, pp. 158-171.

**Lee, B. Y.; Iijima, T.** (2010): High-frequency piezoelectric displacement of PZT films measured using twin-beam laser doppler vibrometer. *Nippon Seramikkusu Kyokai Gakujutsu Ronbunshi/Journal of the Ceramic Society of Japan*, vol. 118, no. 1381, pp. 842-846.

**Lim, Y. Y.; Bhalla, S.; Soh, C. K.** (2006): Structural identification and damage diagnosis using self-sensing piezo-impedance transducers. *Smart Materials and Structures*, vol. 15, no. 4, pp. 987.

**MathWorks** (2015): MatLab 2015a. <https://uk.mathworks.com/products/matlab.html>.

**Mertikas, S. P.** (1985): Error distributions and accuracy measures in navigation: An overview. *Technical Report*, no. 113.

**Na, S.; Lee, H. K.** (2012): A technique for improving the damage detection ability of the electro-mechanical impedance method on concrete structures. *Smart Materials and Structures*, vol. 21, no. 8.

**Park, S.; Ahmad, S.; Yun, C. B.; Roh, Y.** (2006): Multiple crack detection of concrete structures using impedance-based structural health monitoring techniques. *Experimental Mechanics*, vol. 46, no. 5, pp. 609-618.

**PI Ceramic GmbH** (2014): Fundamentals of Piezo technology. *PI Ceramic Piezo Technology*.

**Polytec GmbH** (2010): *Polytec Scanning Vibrometer Theory Manual*.

**Providakis, C.; Liarakos, E.** (2011): T-WiEYE: An early-age concrete strength development monitoring and miniaturized wireless impedance sensing system, in *Procedia Engineering*, vol. 10, pp. 484-489.

**Providakis, C. P.; Liarakos, E. V.; Kampianakis, E.** (2013): Nondestructive wireless monitoring of early-age concrete strength gain using an innovative electromechanical impedance sensing system. *Smart Materials Research*, vol. 2013, pp. 1-10.

**Providakis, C.; Tsistrakis, S.; Voutetaki, M.; Tsompanakis, Y.; Stavroulaki, M. et al.** (2015): A new damage identification approach based on impedance-type measurements and 2D error statistics. *Structural Monitoring and Maintenance*, vol. 2, no. 4.

- Providakis, C.; Tsistrakis, S.; Voutetaki, M.; Tsompanakis, Y.; Stavroulaki, M. et al.** (2016): An innovative active sensing platform for wireless damage monitoring of concrete structures. *Bentham Science Publishers*, pp. 49-62.
- Quinn, W.; Kelly, G.; Barrett, J.** (2012): Development of an embedded wireless sensing system for the monitoring of concrete. *Structural Health Monitoring*, vol. 11, no. 4.
- Ribeiro, M.** (2004): Gaussian probability density functions: Properties and error characterization. *Institute for Systems and Robotics, Technical Report*, pp. 1-30.
- Siringoringo, D. M.; Fujino, Y.** (2006): Experimental study of laser Doppler vibrometer and ambient vibration for vibration-based damage detection. *Engineering Structures*, vol. 28, no. 3, pp. 1803-1815.
- Soh, C. K.; Tseng, K. K. H.; Bhalla, S.; Gupta, A.** (2000): Performance of smart piezoceramic transducers in health monitoring of RC bridge. *Smart Materials and Structures*. <http://iopscience.iop.org/article/10.1088/0964-1726/9/4/317/meta>.
- Sohn, H.; Allen, D. W.; Worden, K.; Farrar, C. R.** (2003): Structural damage classification using extreme value statistics. *Journal of Dynamic Systems, Measurement, and Control*, vol. 127, pp. 125-132.
- Song, G.; Gu, H.; Mo, Y. L.; Hsu, T. T. C.; Dhonde, H.** (2007): Concrete structural health monitoring using embedded piezoceramic transducers. *Smart Materials and Structures*. <http://iopscience.iop.org/article/10.1088/0964-1726/16/4/003/meta>.
- Tawie, R.; Lee, H. K.** (2010): Monitoring the strength development in concrete by EMI sensing technique. *Construction and Building Materials*, vol. 24, no. 9.
- Tawie, R.; Lee, H. K.** (2011): Characterization of cement-based materials using a reusable piezoelectric impedance-based sensor. *Smart Materials and Structures*. <http://iopscience.iop.org/article/10.1088/0964-1726/20/8/085023/meta>.
- Tseng, K. K.; Wang, L.** (2004): Smart piezoelectric transducers for in situ health monitoring of concrete. *Smart Materials and Structures*, vol. 13, no. 5.
- Wang, D.; Song, H.; Zhu, H.** (2013): Numerical and experimental studies on damage detection of a concrete beam based on PZT admittances and correlation coefficient. *Construction and Building Materials*, vol. 49, pp. 564-574.
- Yang, Y.; Divsholi, B. S.** (2010): Sub-frequency interval approach in electromechanical impedance technique for concrete structure health monitoring. *Sensors*, vol. 10, no. 12, pp. 11644-11661.
- Yang, Y.; Divsholi, B. S.; Soh, C. K.** (2010): A reusable PZT transducer for monitoring initial hydration and structural health of concrete. *Sensors*, vol. 10, no. 5, pp. 5193-5208.
- Yang, Y.; Hu, Y.; Lu, Y.** (2008): Sensitivity of PZT impedance sensors for damage detection of concrete structures. *Sensors*, vol. 8, no. 1, pp. 327-346.
- Yu, L.; Tian, Z.** (2013): Lamb wave structural health monitoring using a hybrid pzt-laser vibrometer approach. *Structural Health Monitoring*, vol. 12, no. 5-6.